Ultramicroscopy 180 (2017) 173–179

Contents lists available at ScienceDirect

Ultramicroscopy

journal homepage: www.elsevier.com/locate/ultramic

Electron ptychographic phase imaging of light elements in crystalline materials using Wigner distribution deconvolution

Hao Yang[a], Ian MacLaren[b], Lewys Jones[c], Gerardo T. Martinez[c], Martin Simson[d], Martin Huth[d], Henning Ryll[e], Heike Soltau[d], Ryusuke Sagawa[f], Yukihito Kondo[f], Colin Ophus[a], Peter Ercius[a], Lei Jin[g], András Kovács[g], Peter D. Nellist[c,*]

[a] Molecular Foundry, Lawrence Berkeley National Laboratory, Berkeley, CA, 94720, USA
[b] School of Physics and Astronomy, University of Glasgow, Glasgow G12 8QQ, UK
[c] Department of Materials, University of Oxford, Parks Road, Oxford, OX1 3PH, UK
[d] PNDetector GmbH, Otto-Hahn-Ring 6, München 81739, Germany
[e] PNSensor GmbH, Otto-Hahn-Ring 6, München 81739, Germany
[f] JEOL Ltd.,3-1-2 Musashino Akishima Tokyo 196–8558 Japan
[g] Ernst Ruska–Centre (ER-C) for Microscopy and Spectroscopy with Electrons, Forschungszentrum Jülich GmbH, Jülich 52425, Germany

ARTICLE INFO

Article history:
Received 31 October 2016
Revised 9 February 2017
Accepted 18 February 2017
Available online 1 April 2017

Keywords:
4D-STEM
Pixelated detectors
Ptychography
Phase retrieval
Wigner distribution deconvolution

ABSTRACT

Recent development in fast pixelated detector technology has allowed a two dimensional diffraction pattern to be recorded at every probe position of a two dimensional raster scan in a scanning transmission electron microscope (STEM), forming an information-rich four dimensional (4D) dataset. Electron ptychography has been shown to enable efficient coherent phase imaging of weakly scattering objects from a 4D dataset recorded using a focused electron probe, which is optimised for simultaneous incoherent Z-contrast imaging and spectroscopy in STEM. Therefore coherent phase contrast and incoherent Z-contrast imaging modes can be efficiently combined to provide a good sensitivity of both light and heavy elements at atomic resolution. In this work, we explore the application of electron ptychography for atomic resolution imaging of strongly scattering crystalline specimens, and present experiments on imaging crystalline specimens including samples containing defects, under dynamical channelling conditions using an aberration corrected microscope. A ptychographic reconstruction method called Wigner distribution deconvolution (WDD) was implemented. Experimental results and simulation results suggest that ptychography provides a readily interpretable phase image and great sensitivity for imaging light elements at atomic resolution in relatively thin crystalline materials.

1. Introduction

One of the current authors (PDN) had the great privilege of being in the Cavendish Laboratory at the same time that Ondrej Krivanek and his long-time collaborator Niklas Dellby, arrived to start their initial experiments on spherical aberration correction in scanning transmission electron microscopy (STEM). This was in 1996. At that time, there was deep scepticism regarding whether aberration-correction was possible. A very thorough review article has been written by Hawkes [1], and we will not describe the history of aberration correction here. It suffices to say that it had rather acquired the reputation of being a career killer with funding agencies very reluctant to touch it. Krivanek rightly predicted that the impact of aberration correction would be greatest in STEM, and focused his efforts entirely on that mode. This allowed him to use the quadrupole-octupole route for aberration correction because it was not necessary to correct off-axial aberrations in the way that the corrector designed by Rose [2] and created by Haider was able to do. It became apparent to PDN that the Krivanek and Dellby project was really making progress and had a viable approach to overcoming the challenges that had previously existed. After 50 years, aberration correction was becoming closer to reality. In 2000, PDN joined Nion, the company founded by Krivanek and Dellby, and had a wonderful 4 years learning how to design aberration correctors and contributing to the design of the 5th-order corrector [3]. Although Nion correctors were being shipped for retrofitting to existing VG microscopes, the focus of the company at that time was the design of an entirely new STEM, which has become the Nion UltraSTEM. A highlight of the Nion milestones during those years for PDN was his involvement in the

* Corresponding author.
E-mail address: peter.nellist@materials.ox.ac.uk (P.D. Nellist).

http://dx.doi.org/10.1016/j.ultramic.2017.02.006

successful attempt to resolve the atomic columns in the Si⟨112⟩ lattice with a resolution better than 78 pm [4].

Most STEM imaging modes, such as annular dark-field (ADF) and spectroscopic mapping, can be regarded as being incoherent in which the effective point-spread function for imaging is simply the intensity of the illuminating probe. The only way to improve resolution, and indeed also the signal to noise in analytical signals at high spatial resolution, is through improvement in optics, and this is part of the explanation of why aberration correction has been so important in STEM, and why Krivanek's contribution has been so important. For light elements, however, phase contrast imaging offers the most effective way of imaging light elements while minimising sample damage [5]. Conventional phase contrast imaging with electrons is achieved in a conventional transmission electron microscope (CTEM) with deliberately injected aberrations, which serves as an approximation to a phase plate to convert phase shift to image intensity. The use of such aberrations is therefore incompatible with the optimal conditions for simultaneous incoherent imaging. Furthermore, the relatively small bright-field (BF) detector required for conventional phase contrast in STEM is inefficient and only detects a fraction of the transmitted electrons. The imaging of light elements in STEM can be significantly improved through detector geometry innovations, for example, using an annular detector to form annular bright field (ABF) imaging [6,7] and a segmented detector for differential phase contrast (DPC) imaging [8–10]. However, both a single detector like BF or ABF and segmented detectors like DPC integrate scattered signals in the STEM detector plane, and information is lost. For example, the phase contrast transfer of DPC is known to depend on the partition direction of the quadrant segments [9]. The aim here is to make full use of the intensity variations in the STEM detector plane to provide efficient phase imaging simultaneously with incoherent STEM imaging modes.

Ptychography is known as an efficient approach for extracting phase information from diffraction patterns from spatially limited areas of illumination. First developed by Hoppe back in 1969 [11], ptychography has been used in both X-ray and electron microscopy [12–14]. The first atomic resolution electron ptychography image was demonstrated in 1995 [15], however, with limited field of view due to slow camera speed. A largely defocused probe can reduce the number of diffraction patterns per illuminated area with a sufficient overlap for solving the phase ambiguity. Both the complex transmission function and the probe function can be retrieved iteratively [12,16–18]. This approach has been well adopted by X-ray microscopy especially, however, the largely defocused probe is undesirable in high resolution electron microscopy because it is incompatible with well established incoherent Z-contrast imaging and spectroscopic methods in STEM. Recent advances in fast pixelated detectors [19,20] have created exciting opportunities for electron ptychography, as diffraction patterns can now be recorded in STEM at every position of a 2D raster scan. When an Angstrom sized focused electron probe and a typical probe sampling rate below half an Angstrom per pixel is used, there is sufficient overlapping areas for information redundancy for phase recovery. Therefore, incoherent Z-contrast imaging and energy-dispersive x-ray spectroscopy (EDS) signals can be acquired simultaneously with ptychographic phase imaging [21,22]. The ptychographic phase is shown to give a simple and more efficient phase contrast transfer function (PCTF) than any existing phase contrast imaging modes in STEM [23].

In this work, we use a fast pixelated detector and apply electron ptychography for atomic resolution imaging of crystalline specimens to make use of its high sensitivity for imaging light elements. The ptychography reconstruction method assumes that the sample can be described by a multiplicative transmission function. This conditions is unlikely to be satisfied by the crystalline samples used here which are likely to show dynamical scattering effects. The aim of the paper is to determine whether ptychography can nonetheless provide a useful way of imaging light elements in crystals.

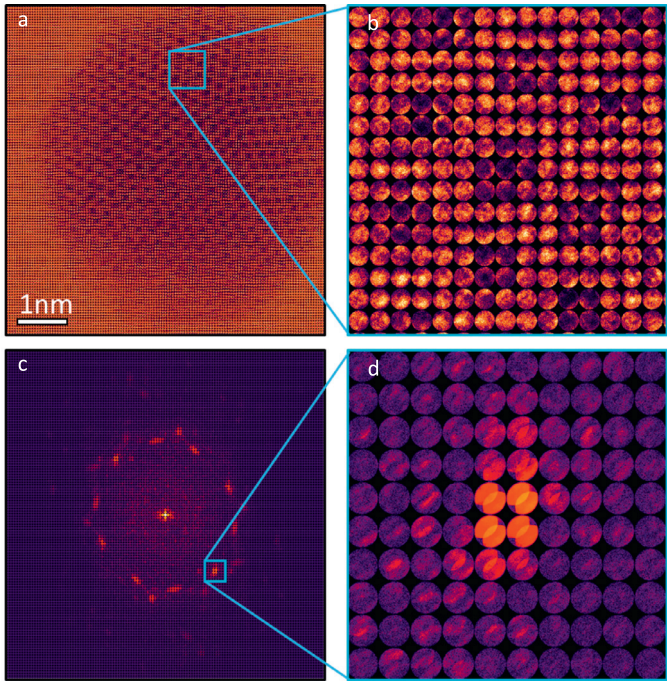

Fig. 1. 4D Ptychography dataset acquired using a fast camera using a STEM. (a) A 2D diffraction pattern is captured at each spatial location across a 2D raster scan over an Au nanoparticle on a carbon support. (b) 2D diffraction patterns from a sub-area of several Au atomic columns. (c) After Fourier transform of the entire 4D dataset with respect to the probe spatial locations, the 2D diffraction patterns become complex values, and the modulus are shown at each spatial frequency of the 2D probe positions. (d) A sub-area of (c) showing the modulus of the diffraction plane signals at spatial frequencies around a 200 diffraction spot.

2. Experimental setup

The experiments in this work were performed using a pnCCD (S)TEM camera [19], a direct electron radiation-hard pixelated detector from PNDetector GmbH, mounted on a JEOL ARM200CF aberration corrected microscope. This camera delivers a readout speed of 1000 full frames per second (fps) with a full frame of 264× 264 detector pixels, and up to 20,000 fps through binning/windowing. For a typical STEM scanning consisting of 256× 256 real space probe positions, a 4D dataset consisting of 66× 264 pixel diffraction patterns (detector binned by 4 in one direction) for each probe position can be recorded in about 16 s. The camera offers a dynamic range wide enough to record both the bright field and dark field signals with single electron sensitivity. Ptychography can be performed with as few as 3 segments in the detector covering the bright-field disc [24], but Yang et al. [23] suggest that 16× 16 detector pixels or higher makes the most efficient use of how the signal is expressed in the detector plane, and high pixelation also allows correction of residual aberrations [21]. The experiments were therefore optimised to have the largest number of pixels for the bright field signal. The dark field signal was recorded simultaneously using an annular dark field (ADF) detector to form a simultaneous incoherent Z-contrast image.

Fig. 1 shows a schematic illustration of the recorded 4D dataset. All data was recorded with the focus manually set to optimise the ADF image contrast, which should be close to the probe being focused on the entrance surface. A 2D diffraction pattern is captured at each spatial location across a 2D raster scan over

an Au nanoparticle on a carbon support. When the 2D diffraction patterns are tiled based on their probe spatial locations for the visualisation purpose, the intensity variation in the diffraction patterns already reveals the atomic structure of the Au nanoparticle in Fig. 1a. A magnified sub-area of a few Au atomic columns in Fig. 1b shows diffraction patterns consisting of only bright field diffraction discs. The bright field diffraction intensities are weaker on the Au columns than those between the Au columns because electrons are scattered to higher angles by the Au columns. Such intensity variations in the diffraction patterns as a function of probe positions carry rich information about specimen induced phase changes of the incident electron wave as it propagates through the specimen. Thanks to the fast pixelated detectors being able to record diffraction patterns from a large number of probe positions, a typical sampling rate for conventional STEM imaging (0.2 Å for the example in Fig. 1) will guarantee a sufficient sampling for the ptychographic reconstruction method used here.

3. Theoretical background

The ptychography method used in this work is a fast non-iterative method called Wigner-distribution deconvolution (WDD), which was first introduced in the early 1990s [13,25] and recently has been further developed [21,26,27]. Compared to the single-side band (SSB) approach based on a linear weak phase object approximation (WPOA) [14,22,23], WDD is a full reconstruction that takes into account the non-linear terms through a deconvolution approach. Since WDD does not require the WPOA, a broader range of materials can be reconstructed using WDD compared to SSB. Due to fast pixelated detectors, both WDD and SSB enable the simultaneous acquisition of an incoherent Z-contrast image using an annular dark field detector (ADF) along with the ptychographic phase imaging. This has been demonstrated to be highly beneficial because it provides the sensitivity to both heavy and light elements simultaneously at atomic resolution [21]. In addition, WDD has recently been shown to allow a direct measurement and correction of residual lens aberrations in the phase image through post-acquisition processing [21]. It provides depth sensitivity for extracting three dimensional structure information along the e-beam direction, without tilting the specimen or changing the defocus of the electron probe.

This section outlines the theoretical background and procedures for WDD applied to the 4D dataset as shown in Fig. 1. At the micro-diffraction plane, the electron wave $M(\mathbf{K_f}, \mathbf{R_p})$ can be described as the Fourier transform of the product between the real space probe function $a(\mathbf{R}-\mathbf{R_p})$ and the real space object function $\psi(\mathbf{R})$ under the phase object approximation, as shown in Eq. (1). $a(\mathbf{R})$ can be calculated by forward Fourier transform of the probe function $A(\mathbf{K_f})$ at the probe-forming aperture plane. The modulus of $A(\mathbf{K_f})$ is a top-hat function and the phase of $A(\mathbf{K_f})$ is influenced by the presence of lens aberrations of the microscope. $\mathbf{R_p}$ is the two dimensional coordinates of the probe with respect to the specimen in real space. The recorded diffraction pattern intensity is simply the modulus square of $M(\mathbf{K_f}, \mathbf{R_p})$.

$$M(\mathbf{K_f}, \mathbf{R_p}) = \int a(\mathbf{R}-\mathbf{R_p})\psi(\mathbf{R})exp(i2\pi\mathbf{K_f}\cdot\mathbf{R})d\mathbf{R} \quad (1)$$

The first step of WDD as well as SSB is to take a two dimensional Fourier transform of the 4D dataset with respect to the spatial location of the probe $\mathbf{R_p}$, which transforms the 4D dataset into a new complex-valued 4D dataset $G(\mathbf{K_f}, \mathbf{Q_p})$, as expressed in Eq. (2). $G(\mathbf{K_f}, \mathbf{Q_p})$ is expressed as a function of two reciprocal space vectors, the scattering angle $\mathbf{K_f}$ and the spatial frequency of probe positions $\mathbf{Q_p}$. This Fourier transform in Eq. (2) was first proposed by Rodenburg et al. [14], which follows the original idea of ptychography first introduced by Hoppe in 1969 [11] to retrieve the relative phase between neighboring probe positions. The modulus of the complex 4D dataset $G(\mathbf{K_f}, \mathbf{Q_p})$ is shown in Fig. 1c, where the detector plane is tiled as a function of the probe spatial frequency. Strong modulus can be seen at the diffracted discs, as shown in Fig. 1d.

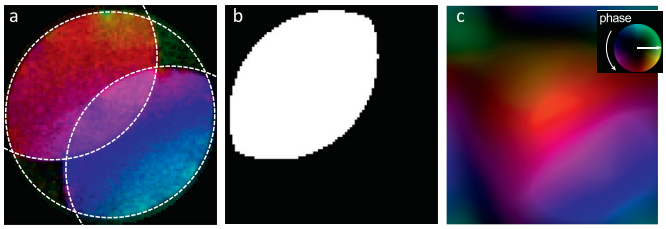

Fig. 2. Schematic illustration of the Wigner distribution deconvolution (WDD) procedure. (a) The complex 4D dataset $G(\mathbf{K_f}, \mathbf{Q_p})$ at a single probe spatial frequency $\mathbf{Q_p}$ (as shown in Fig. 1d) shows beam interferences at the detector plane between the undiffracted central beam and two diffracted first order beams, as indicated by dashed circles. (b) The Fourier transform of the Wigner distribution function of the probe function, i.e., $A(\mathbf{K_f})A^*(\mathbf{K_f}+\mathbf{Q_p})$. In the case of zero lens aberration, it's the overlapping region of two top-hat aperture functions. After deconvolving (b) from (a), the Fourier transform of the Wigner distribution function of the object, i.e., $\Psi(\mathbf{K_f})\Psi^*(\mathbf{K_f}-\mathbf{Q_p})$ is shown in (c). The modulus and phase are combined in (a) and (c), with the phase represented by color and modulus by brightness, as indicated on the color wheel scale. Figure (a)–(c) are shown in the detector $\mathbf{K_f}$ plane, with $\mathbf{K_f}=0$ located at the center of each figure.

$$\begin{aligned} G(\mathbf{K_f}, \mathbf{Q_p}) &= \mathcal{F}_{\mathbf{R_p}}[|M(\mathbf{K_f}, \mathbf{R_p})|^2] \\ &= A(\mathbf{K_f})A^*(\mathbf{K_f}+\mathbf{Q_p}) \otimes_{\mathbf{K_f}} \Psi(\mathbf{K_f})\Psi^*(\mathbf{K_f}-\mathbf{Q_p}) \end{aligned} \quad (2)$$

where $\Psi(\mathbf{Q_p})$ is the Fourier transform of the object transmission function as a function of the probe spatial frequency $\mathbf{Q_p}$ and would be the scattered wavefunction under conditions of plane-wave illumination.

Applying WPOA to Eq. (2) will lead us to the SSB ptychography method, where $G(\mathbf{K_f}, \mathbf{Q_p})$ is approximated as a linear function of the interference between the direct electron beam $A(\mathbf{K_f})$ and two first order diffracted beams $A(\mathbf{K_f} \pm \mathbf{Q_p})$ in Eq. (3) [14]. The phase $\Psi(\mathbf{Q_p})$ can be simply integrated from either side of the overlapping discs $A(\mathbf{K_f})A^*(\mathbf{K_f}+\mathbf{Q_p})$ assuming zero lens aberrations [22].

$$\begin{aligned} G(\mathbf{K_f}, \mathbf{Q_p}) = {} & |A(\mathbf{K_f})|^2\delta(\mathbf{Q_p}) + A(\mathbf{K_f})A^*(\mathbf{K_f}+\mathbf{Q_p})\Psi^*(-\mathbf{Q_p}) \\ & + A^*(\mathbf{K_f})A(\mathbf{K_f}-\mathbf{Q_p})\Psi(+\mathbf{Q_p}) \end{aligned} \quad (3)$$

The SSB approach is very simple, and is only possible because of the availability of aberration correctors. An experimental example of $G(\mathbf{K_f}, \mathbf{Q_p})$ representing the interferences between the undiffracted and diffracted beams is illustrated in Fig. 2a, where the full dashed circle indicates the bright field disc in the diffraction plane and two shifted discs ($\pm$ $\mathbf{Q_p}$) overlap with the bright field disc.

Without using the WPOA, Eq. (2) expresses the complex 4D dataset as a convolution between two terms that are functions of only the probe and the object, respectively. If the probe function is known, then the object function can be separated from the probe function through deconvolution. This means that the influence of any known geometrical lens aberrations of the probe can be separated from the object function. Because the two terms are convolved in the detector plane ($\mathbf{K_f}$), it is a natural step to apply an inverse Fourier transform to $G(\mathbf{K_f}, \mathbf{Q_p})$ in Eq. (2) with respect to $\mathbf{K_f}$, another complex 4D dataset denoted as $H(\mathbf{R}, \mathbf{Q_p})$ in the following [13]:

$$\begin{aligned} H(\mathbf{R}, \mathbf{Q_p}) &= \mathcal{F}^{-1}_{\mathbf{K_f}}[G(\mathbf{K_f}, \mathbf{Q_p})] \\ &= \int a^*(\mathbf{b})a(\mathbf{b}+\mathbf{R})exp(-i2\pi\mathbf{Q_p}\cdot\mathbf{b})d\mathbf{b} \\ &\quad \cdot \int \psi^*(\mathbf{c})\psi(\mathbf{c}+\mathbf{R})exp(i2\pi\mathbf{Q_p}\cdot\mathbf{c})d\mathbf{c} \end{aligned} \quad (4)$$

It turns out that the two integrals in Eq. (4) follow the mathematical definition of a Wigner distribution function:

$$\chi_q(\mathbf{a},\mathbf{b}) = \int q^*(\mathbf{c})q(\mathbf{c}+\mathbf{a})exp(i2\pi\,\mathbf{c}\cdot\mathbf{b})d\mathbf{c} \quad (5)$$

Combining Eqs. (4) and(5), the 4D dataset $H(\mathbf{R}, \mathbf{Q_p})$ can be rewritten as:

$$H(\mathbf{R},\mathbf{Q_p}) = \chi_a(\mathbf{R},-\mathbf{Q_p})\cdot\chi_\psi(\mathbf{R},\mathbf{Q_p}) \quad (6)$$

Using Eq. (6), it is relatively straightforward to separate the Wigner distribution function of the probe $\chi_a(\mathbf{R},-\mathbf{Q_p})$ and Wigner distribution function of the object $\chi_\psi(\mathbf{R}, \mathbf{Q_p})$ using a conventional Wiener deconvolution routine.

$$\chi_\psi(\mathbf{R},\mathbf{Q_p}) = \chi_a^*(\mathbf{R},-\mathbf{Q_p})H(\mathbf{R},\mathbf{Q_p})/(|\chi_a(\mathbf{R},-\mathbf{Q_p})|^2+\epsilon), \quad (7)$$

where ϵ is a small constant to avoid dividing by zero values, and its value is around one percent of $|\chi_a(\mathbf{R},-\mathbf{Q_p})|^2$. To reconstruct the specimen image after the deconvolution, we need to perform another Fourier transform on $\chi_\psi(\mathbf{r}, \mathbf{Q_p})$ along $\mathbf{r}$ as follows:

$$D(\mathbf{K_f},\mathbf{Q_p}) = \mathcal{F}_{\mathbf{K_f}}[\chi_\psi(\mathbf{R},\mathbf{Q_p})] = \Psi(\mathbf{K_f})\Psi^*(\mathbf{K_f}-\mathbf{Q_p}) \quad (8)$$

To illustrate the deconvolution process, Fig. 2b shows the aperture overlapping function as described in Eq. (2). Under zero lens aberrations this function has a shape that corresponds to the overlapping area between the bright field disc $A(\mathbf{K_f})$ and the shifted disc $A(\mathbf{K_f}+\mathbf{Q_p})$. After Wiener deconvolution, $D(\mathbf{K_f}, \mathbf{Q_p})$ at this particular probe spatial frequency $\mathbf{Q_p}$ is shown in Fig. 2c. $D(\mathbf{K_f}, \mathbf{Q_p})$ is a complex 4D dataset resulting from the deconvolution, and it is a function of only $\Psi(\mathbf{Q_p})$. A direct and simplified solution to calculate $\Psi(\mathbf{Q_p})$ from $D(\mathbf{K_f}, \mathbf{Q_p})$ is to slice through the 4D dataset $D(\mathbf{K_f}, \mathbf{Q_p})$ at the plane of $\mathbf{K_f}=0$, which leads to a solution of $\Psi(\mathbf{Q_p})$ as following,

$$\Psi(\mathbf{Q_p}) = D^*(0,\mathbf{Q_p})/\sqrt{D(0,0)} \quad (9)$$

Eq. (9) is found to work well for weak phase objects [21] and thin crystalline specimens in this work, although under extremely low electron doses, the Wiener filter approach in this work may not be the best solution, and there is still plenty room for improvement in future work in terms of extracting phase information from the information redundant 4D dataset $D(\mathbf{K_f}, \mathbf{Q_p})$.

4. Results and discussions

Fig. 3 shows an experimental result of simultaneous ADF, ABF and ptychographic phase images of an Au nanoparticle with a fivefold twinning on a carbon support, reconstructed from the same 4D dataset as shown in Fig. 1. Reconstructed phase images using both SSB and WDD methods are shown. As expected, better contrast of the carbon support is shown in both ABF and the two ptychography phase images, compared to the ADF image in Fig. 3a. A close comparison between ABF and the ptychographic phase images suggest the contrast of the thin edge of the Au nanoparticle at the bottom of the ABF image is not as clear as in the ptychographic phase images, and this is because ABF is a nonlinear imaging method which is very sensitive to the focusing condition and sample thickness, and recent studies suggest that ABF has no phase contrast transfer for weak phase objects under zero lens aberrations [22,23]. Compared to the SSB phase, the WDD phase shows a better contrast and much higher quantitative phase values, and this is because the Au nanoparticle no longer satisfies the WPOA used by SSB.

A significant advantage of WDD compared to SSB is its ability to correct residual lens aberrations. The phase information redundancy in the 4D dataset enables a sensitivity for diagnosing and correcting small residual lens aberrations [21]. Fig. 4 shows an example of resolution improvement using a sample of Au nanoparticles on carbon support. For this sample, high resolution phase

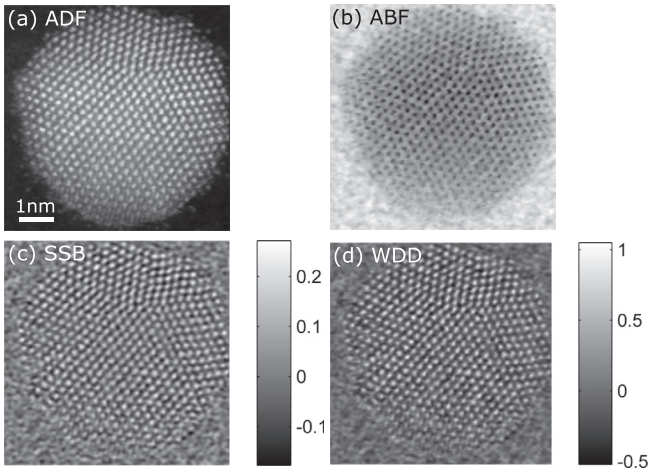

Fig. 3. Imaging a gold nanoparticle on a thin carbon support using (a) simultaneous ADF, (b) synthetic ABF, ptychography SSB phase and WDD phase. Colorbar in (c,d) in unit of radian. The synthetic ABF has a collection angle of 7.2–14.4 mrads in (b). The diffraction patterns were recorded using 264× 264 detector pixels at 1000 frames per second speed.

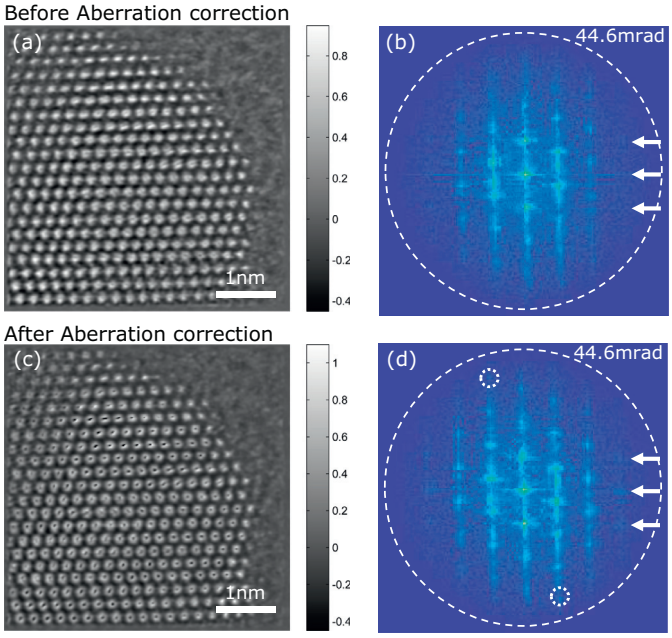

Fig. 4. The phase image of the complex transmission function reconstructed using ptychography WDD (a) before and (c) after post-acquisition aberration correction. The Fourier transform of the complex phase images are shown in (b) and (d), respectively. The arrows point to diffraction spots that are not visible before aberration correction, but become visible after aberration correction. The $4\bar{4}2$ diffraction spots indicated by the small dashed circles in (d) corresponds to a reciprocal scattering angle of 39 mrad and a real space spacing of 0.68 Å. The big dashed circles indicates the diffraction limited resolution of 44.6 mrad, which is twice the convergence semi-angle of the probe forming aperture. The diffraction patterns were recorded using 66× 264 detector pixels at 4000 frames per second speed.

information up to 0.68 Å was achieved, as shown in Fig. 4d, and the visibility of some high order diffraction spots (indicated by arrows and dashed circles) is much improved compared to without aberration correction in Fig. 4b. Fine details in the phase profile of individual atomic columns become visible after applying post-acquisition aberration correction in Fig. 4c compared to without aberration correction in Fig. 4a. A decrease in phase values in the center of many Au atomic columns in Fig. 4c is observed, which is likely to be due to channelling impacting on the ptychographical

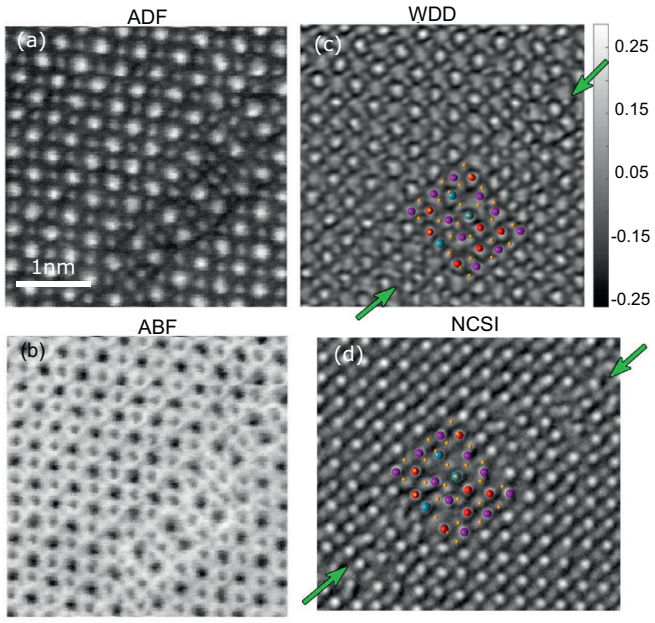

Fig. 5. HAADF, synthetic ABF and the reconstructed phase of an antiphase boundary in Ti, Nd doped BiFeO3. It should be noted that the oxygen positions which are invisible in the HAADF image are labelled as small yellow spheres in the phase image. The B-site Fe columns are labelled as larger red spheres, the B-site Ti columns are labelled as blue spheres, and the A-site (Bi/Nd) columns are labelled as bright purple spheres. The synthetic ABF has a collection angle of 11.0–22.0 mrads in (c). The diffraction patterns were recorded using 66× 264 detector pixels at 4000 frames per second speed. (For interpretation of the references to colour in this figure legend, the reader is referred to the web version of this article.)

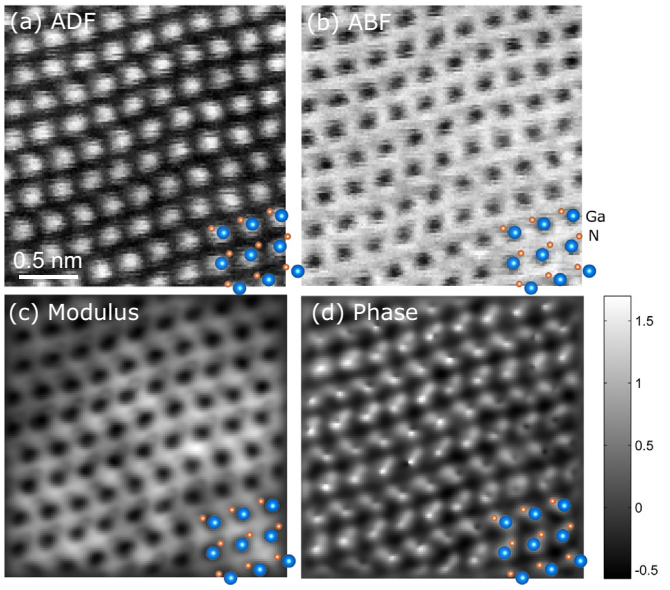

Fig. 6. Simultaneous ADF, synthetic ABF, and the reconstructed modulus and phase of bulk GaN imaged along [21$\bar{1}$0]. The probe forming aperture is around 14.4 mrads, and the synthetic ABF has a collection angle of 7.2–14.4 mrads. The diffraction patterns were recorded using 66× 264 detector pixels at 4000 frames per second speed.

reconstruction. Ptychography is known for its "double-resolution" and furthermore for its ability to retrieve phase information beyond the conventional information limit imposed by the partial coherence of the electron wave [13,28] using a so-called "stepping-out" procedure. In this work, the "stepping-out" procedure is not implemented, but the 0.68 Å resolution is approaching the diffraction limited resolution of 0.56 Å using the 22.3 mrads convergence semi-angle probe forming aperture.

Atomic resolution imaging of light elements in crystalline specimens can also be achieved using the negative-spherical-aberration (Cs) imaging (NCSI) in TEM [29,30] or ABF [7] in STEM. Here we show that ptychography WDD phase imaging also provides an excellent sensitivity for imaging light elements. Fig. 5 shows an experimental result of a $BiFeO_3$ anti-phase grain boundary. A ceramic sample $Bi_{0.85}Nd_{0.15}Fe_{0.9}Ti_{0.1}O_3$ (nominal composition) was prepared by a conventional mixed oxide procedure as described previously [31]. A suitable specimen thin enough for phase contrast imaging (less than 5 nm thick with minimal surface damage) was made by a FIB liftout method, followed by argon ion milling at 500V with a Fischione Nanomill. We show that WDD phase provides a sensitive and readily interpretable phase contrast for light elements in crystalline specimens. The specimen has charged antiphase domain boundaries of Nd, Ti doped $BiFeO_3$ [32,33], and here we show a direct comparison of WDD phase with both the synthetic ABF and a NCSI result from the same specimen. HRTEM was performed using the negative-C_S imaging (NCSI) technique using a FEI Titan 80–300, operated at 300 kV using a spherical aberration C_S value of -12μm and a small positive defocus of a few nm, tuned to give the best possible positive contrast for all atoms simultaneously [30]. Images were recorded using a Gatan Ultrascan 1000P camera. Oxygen columns are not visible in the HAADF image, and barely visible in the ABF image. In comparison, the oxygen columns are clearly visible in both the bulk and the domain boundary in both the WDD phase and the NCSI image. The simultaneous Z-contrast image provides a good reference image for identifying the composition of each atomic column. In the WDD phase image, the Bi columns show the strongest phase values compared to the Fe/Ti columns and the oxygen columns. No phase wrapping or contrast reversal occurs, which perhaps is expected from a very thin specimen of less than 5nm thick. Longer range fields that may arise from the boundary charge are not apparent in the phase image, which may be due to the weaker transfer at low spatial frequencies, and detection of these fields may require a much smaller convergence angle and is the subject of further work.

Fig. 6 shows another experimental example of imaging GaN along [21$\bar{1}$0]. The ADF image shows contrast only from the Ga columns, and the contrast of N columns in the ABF image is difficult to identify as well. In comparison, the Ga-N dumbbells are clearly resolved in the reconstructed phase image in Fig. 6d. The modulus in Fig. 6c also shows a visible but weak contrast of the N column. Slightly different from the $BiFeO_3$ case, the relatively heavy Ga columns don't show a much higher phase value than the N columns, and in some places the Ga column shows a weaker contrast than the N column. For a better understanding of the ptychographic phase contrast, we compare the GaN experimental results with multislice image simulations of a series of specimen thicknesses up to 17.5 nm (55 unit cells), as shown in Fig. 7. It can be seen that the phase of the relatively heavy Ga starts to become wrapped and contrast reversal occurs as the specimen thickness increases to over 6.4 nm (20 unit cells), and the phase of Ga wraps back as thickness keeps increasing.

A detailed comparison of the sensitivity to light elements of ABF and ptychography, and how they response to focus and thickness changes is for future work. Even with the recent camera developments, the probe dwell times for STEM ptychography are still considerably longer than for single channel detectors, and it is possible that the probe scan instabilities have reduced the N column visibility in the ABF image in Figs. 5 and6, and also caused the contrast reversals in the ptychography phase image in Fig. 6.

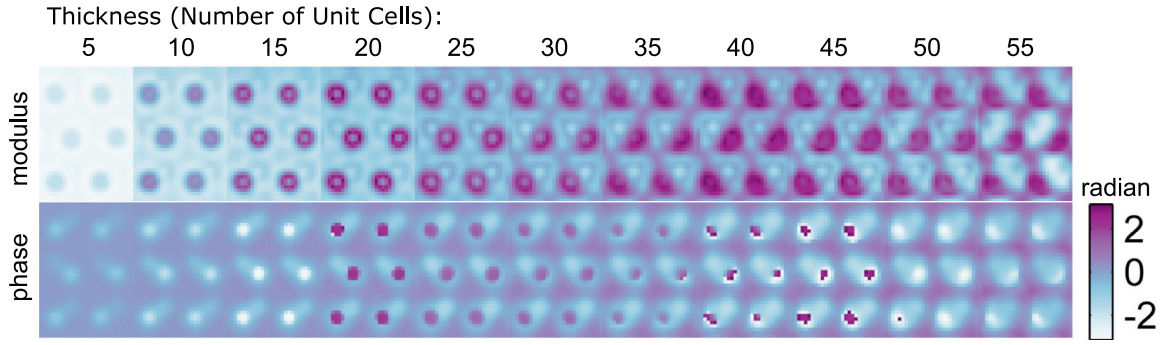

Fig. 7. Reconstructed modulus and phase of GaN along [21$\bar{1}$0] using simulated 4D dataset of different specimen thicknesses. Multislice frozen phonon simulations were used for the simulation, and the same microscope parameters as the experiment were used.

5. Conclusion

In conclusion we have shown that using a pnCCD pixelated detector, a highly efficient phase contrast imaging mode may be achieved by applying ptychography to the 4D STEM datasets, which is complementary to the well established incoherent Z-contrast imaging in STEM. Experimental results and simulations suggest that this unique imaging mode which combines WDD ptychographic phase and Z-contrast imaging offers readily interpretable imaging of both light and heavy atomic columns in crystalline specimens. In the experimental examples shown here, the WDD phase results show a stronger contrast of light elements than that of ABF. A detailed comparison of the sensitivity to light elements of ABF and ptychography, and how they response to focus and thickness changes is for future work. Being able to correct aberrations through post processing to improves the resolution of the reconstructed phase offers additional advantages compared to existing phase contrast imaging methods in STEM.

The ability of the WDD ptychographic approach to reconstruct useful images from crystals may be regarded as somewhat surprising. The theoretical approach laid out in Section 3 relied on a multiplicative sample scattering function. All the examples shown here would be expected to exhibit dynamical scattering behaviour, and therefore violate the multiplicative approximation. It is therefore intriguing that WDD ptychography is an effective way of forming phase images of crystalline specimens in STEM. A more detailed explanation of this effect is under study. The aim here was to explore whether ptychographically retrieved phase images of crystals offered useful images, which does appear to be the case. Future work will examine the theoretical basis of this in detail, and will also explore whether the ptychographical approach can be adapted to cope with dynamical scattering conditions, for example through an inverse multislice approach [34].

Acknowledgements

The authors acknowledge funding from the EPSRC (grant EP/K032518/1, EP/K040375/1, EP/M009963/1 and EP/M010708/1) and the EU FP7 Grant Agreement 312483 (ESTEEM2). Work at the Molecular Foundry was supported by the Office of Science, Office of Basic Energy Sciences, of the U.S. Department of Energy under Contract No. DE-AC02-05CH11231. The raw data is available by contacting PDN (peter.nellist@materials.ox.ac.uk).

References

[1] P.W. Hawkes, The correction of electron lens aberrations, Ultramicroscopy 156 (2015) A1–A64.
[2] H. Rose, Outline of a spherically corrected semiaplanatic medium-voltage transmission electron-microscope, Optik 85 (1990) 19–24.
[3] O.L. Krivanek, P.D. Nellist, N. Dellby, M.F. Murfitt, Z. Szilagyi, Towards sub-0.5 Å electron beams, Ultramicroscopy 96 (2003) 229–237.
[4] P.D. Nellist, M.F. Chisholm, N. Dellby, O.L. Krivanek, M.F. Murfitt, Z.S. Szilagyi, A.R. Lupini, A. Borisevich, W.H. Sides, S.J. Pennycook, Direct sub-angstrom imaging of a crystal lattice, Science 305 (2004) 1741.
[5] R. Henderson, The potential and limitations of neutrons, electrons and x-rays for atomic resolution microscopy of unstained biological molecules, Q. Rev. Biophys. 28 (1995) 171–193.
[6] H. Rose, Phase contrast in scanning transmission electron microscopy, Optik (Stuttg) 39 (1974) 416–436.
[7] S.D. Findlay, N. Shibata, H. Sawada, E. Okunishi, Y. Kondo, Y. Ikuhara, Dynamics of annular bright field imaging in scanning transmission electron microscopy, Ultramicroscopy 110 (2010) 903–923.
[8] N.H. Dekkers, H. De Lang, Differential phase contrast in a STEM, Optik (Stuttg) 41 (1974) 452–456.
[9] H. Rose, Nonstandard imaging methods in electron microscopy, Ultramicroscopy 2 (1977) 251–267.
[10] N. Shibata, S.D. Findlay, Y. Kohno, H. Sawada, Y. Kondo, Y. Ikuhara, Differential phase-contrast microscopy at atomic resolution, Nat. Phys. 8 (2012) 611–615.
[11] W. Hoppe, Beugung im inhomogenen primärstrahlwellenfeld. i. prinzip einer phasenmessung von elektronenbeugungsinterferenzen, Acta Crystallographica Sect. A 25 (1969) 495–501.
[12] P. Thibault, M. Dierolf, A. Menzel, O. Bunk, C. David, F. Pfeiffer, High-resolution scanning x-ray diffraction microscopy, Science 321 (2008) 379–382.
[13] J.M. Rodenburg, R.H.T. Bates, The theory of super-resolution electron microscopy via wigner-distribution deconvolution, Philosophical Transactions of the Royal Society of London A: Mathematical, Phys. Eng. Sci. 339 (1992) 521–553.
[14] J.M. Rodenburg, B.C. McCallum, P.D. Nellist, Experimental tests on double-resolution coherent imaging via STEM, Ultramicroscopy 48 (1993) 304–314.
[15] P.D. Nellist, B.C. McCallum, J.M. Rodenburg, Resolution beyond the 'information limit' in transmission electron microscopy, Nature 374 (1995) 630–632.
[16] A.M. Maiden, J.M. Rodenburg, An improved ptychographical phase retrieval algorithm for diffractive imaging, Ultramicroscopy 109 (2009) 1256–1262.
[17] C.T. Putkunz, A.J. DAlfonso, A.J. Morgan, M. Weyland, C. Dwyer, L. Bourgeois, J. Etheridge, A. Roberts, R.E. Scholten, e.a. K. A. Nugent, Atom-scale ptychographic electron diffractive imaging of boron nitride cones, Phys. Rev. Lett. 108 (2012) 073901.
[18] A.J. D'Alfonso, A.J. Morgan, A.W.C. Yan, P. Wang, H. Sawada, A.I. Kirkland, L.J. Allen, Deterministic electron ptychography at atomic resolution, Phys. Rev. B 89 (2014) 064101.
[19] H. Ryll, M. Simson, R. Hartmann, P. Holl, M. Huth, S. Ihle, Y. Kondo, P. Kotula, A. Liebel, K. Müller-Caspary, A. Rosenauer, R. Sagawa, J. Schmidt, H. Soltau, L. Strüder, A pnCCD-based, fast direct single electron imaging camera for TEM and STEM, J. Instrum. 11 (2016) P04006.
[20] M.W. Tate, P. Purohit, D. Chamberlain, K.X. Nguyen, R. Hovden, C.S. Chang, P. Deb, E. Turgut, J.T. Heron, e.a. D. G. Schlom, High dynamic range pixel array detector for scanning transmission electron microscopy, Microsc. Microanal. 22 (2016) 237–249.
[21] H. Yang, R.N. Rutte, L. Jones, M. Simson, R. Sagawa, H. Ryll, M. Huth, T.J. Pennycook, M.L.H. Green, H. Soltau, Y. Kondo, B.G. Davis, P.D. Nellist, Simultaneous atomic-resolution electron ptychography and z-contrast imaging of light and heavy elements in complex nanostructures, Nat. Commun. 7 (2016) 12532.
[22] T.J. Pennycook, A.R. Lupini, H. Yang, M.F. Murfitt, L. Jones, P.D. Nellist, Efficient phase contrast imaging in STEM using a pixelated detector. part 1: experimental demonstration at atomic resolution, Ultramicroscopy 151 (2015) 160–167.
[23] H. Yang, T.J. Pennycook, P.D. Nellist, Efficient phase contrast imaging in STEM using a pixelated detector. part II: optimisation of imaging conditions, Ultramicroscopy 151 (2015) 232–239.
[24] H.G. Brown, A.J. D'Alfonso, Z. Chen, A.J. Morgan, M. Weyland, C. Zheng, M.S. Fuhrer, S.D. Findlay, L.J. Allen, Structure retrieval with fast electrons using segmented detectors, Phys. Rev. B 93 (2016) 134116.

[25] H.N. Chapman, Phase-retrieval x-ray microscopy by wigner-distribution deconvolution, Ultramicroscopy 66 (1996) 153–172.
[26] P. Li, T.B. Edo, J.M. Rodenburg, Ptychographic inversion via wigner distribution deconvolution: noise suppression and probe design, Ultramicroscopy 147 (2014) 106–113.
[27] J. Lee, G. Barbastathis, Denoised wigner distribution deconvolution via low-rank matrix completion, Opt. Express 24 (2016) 20069–20079.
[28] T. Plamann, J.M. Rodenburg, Electron ptychography. II. theory of three-dimensional propagation effects, Acta Crystallographica Sect. A 54 (1998) 61–73.
[29] C.L. Jia, K. Urban, Atomic-resolution measurement of oxygen concentration in oxide materials, Science 303 (2004) 2001–2004.
[30] C.L. Jia, M. Lentzen, K. Urban, High-resolution transmission electron microscopy using negative spherical aberration, Microsc. Microanal. 10 (2004) 174–184.
[31] K. Kalantari, I. Sterianou, S. Karimi, M.C. Ferrarelli, S. Miao, D.C. Sinclair, I.M. Reaney, Ti-doping to reduce conductivity in $Bi_{0.85}Nd_{0.15}FeO_3$ ceramics, Adv. Funct. Mater. 21 (2011) 3737–3743.
[32] I. MacLaren, L. Wang, O. Morris, A.J. Craven, R.L. Stamps, B. Schaffer, Q.M. Ramasse, S. Miao, K. Kalantari, I. Sterianou, I.M. Reaney, Local stabilisation of polar order at charged antiphase boundaries in antiferroelectric $(Bi_{0.85}Nd_{0.15})(Ti_{0.1}Fe_{0.9})O_3$, APL Mater. 1 (2013) 021102.
[33] I. MacLaren, L. Wang, A.J. Craven, Q.M. Ramasse, B. Schaffer, K. Kalantari, I.M. Reaney, The atomic structure and chemistry of Fe-rich steps on antiphase boundaries in Ti-doped $Bi_{0.9}Nd_{0.15}FeO_3$, APL Mater. 2 (2014) 066106.
[34] A.M. Maiden, M.J. Humphry, J. Rodenburg, Ptychographic transmission microscopy in three dimensions using a multi-slice approach, JOSA A 29 (2012) 1606–1614.